Weak Measurement of Elliptical Dipole Moments by *C*-Point Splitting

Sergey Nechayev,[1,2,*] Martin Neugebauer,[1,2,*] Martin Vorndran,[1,2] Gerd Leuchs,[1,2] and Peter Banzer[1,2,†]
[1]*Max Planck Institute for the Science of Light, Staudtstraße 2, D-91058 Erlangen, Germany*
[2]*Institute of Optics, Information and Photonics, University Erlangen-Nuremberg, Staudtstraße 7/B2, D-91058 Erlangen, Germany*

(Received 16 April 2018; published 13 December 2018)

We investigate points of circular polarization in the far field of elliptically polarized dipoles and establish a relation between the angular position and helicity of these *C* points and the dipole moment. In the case of highly eccentric dipoles, the *C* points of opposite handedness exhibit only a small angular separation and occur in the low intensity region of the emission pattern. In this regard, we introduce an optical weak measurement approach that utilizes the transverse electric (azimuthal) and transverse magnetic (radial) far-field polarization basis. Projecting the far field onto a spatially varying postselected polarization state reveals the angular separation and the helicity of the *C* points. We demonstrate the applicability of this approach and determine the elliptical dipole moment of a particle sitting on an interface by measuring the *C* points in its far field.

DOI: 10.1103/PhysRevLett.121.243903

Introduction.—Dipole emitters such as molecules, quantum dots, and nano-antennas represent fundamental building blocks in nano-optics [1–4]. Their emission characteristics depend on the phases and amplitudes of the three electric and/or magnetic dipolar components. For instance, Huygens dipoles—composed of perpendicular electric and magnetic dipole moments—exhibit directional emission, finding applications in nanolocalization [5] and metasurfaces [6]. As another example, spinning electric or magnetic dipoles couple directionally to spin-momentum-locked modes [7,8], which allows for controlling the flow of light by the direction of the spin [9,10]. Furthermore, the far field of spinning dipoles is split into two half-spaces with opposite signs of helicity [11,12]. The extent of this spin separation is linked to the ellipticity of the dipole [11,12].

In this Letter, we derive a formalism that allows for determining the orientation and ellipticity of dipole moments by measuring the far-field positions and helicities of points of circular polarization (*C* points [13]). Additionally, we resolve these *C* points in the low intensity region of highly eccentric dipoles by applying a method similar to quantum weak measurement (WM) [14,15], which in optics is used for observing beam shift phenomena [16–18] and angular rotations [19,20]. To the best of our knowledge, all optical WM experiments reported to date utilize a homogeneous Cartesian polarization basis. Here, we theoretically show that the far-field projection onto a spatially varying postselected polarization state [21] allows for creating well-separated asymmetric far-field intensity patterns, which indicate the helicity and angular separation of the *C* points and the dipole ellipticity. For demonstration, we measure the ellipticity of a dipole moment induced in a scatterer on a dielectric interface.

Elliptically polarized dipoles in free-space.—The far-field emission of an elliptically polarized dipole in free space, whose dipole moment is, without loss of generality, parallel to the y-z plane, $\mathbf{p} = p_y\mathbf{e}_y + p_z\mathbf{e}_z \equiv |p_y|\mathbf{e}_y + \exp(\imath\Delta\varphi)|p_z|\mathbf{e}_z$, with $\Delta\varphi$ the relative phase between the dipole components, is given by [2,23,24]

$$\mathbf{E} = \begin{pmatrix} E_{\mathrm{TE}} \\ E_{\mathrm{TM}} \end{pmatrix} \propto \hat{M}\mathbf{p} = \begin{pmatrix} \frac{k_x}{k_\perp} & 0 \\ \frac{k_y k_z}{k_\perp k_0} & -\frac{k_\perp}{k_0} \end{pmatrix} \begin{pmatrix} p_y \\ p_z \end{pmatrix}, \quad (1)$$

where k_0 is the wave number in vacuum, $k_\perp = (k_x^2 + k_y^2)^{1/2}$, $k_z = \pm(k_0^2 - k_\perp^2)^{1/2}$, and the sign of k_z depends on the half-space ($z \gtrless 0$). TE and TM indicate transverse electric and transverse magnetic far-field components and the matrix $\hat{M}(k_x, k_y)$ describes the field overlap of the individual plane waves of the angular spectrum with the dipole moment [25]. In the x-z plane ($k_y = 0$), the matrix becomes diagonal:

$$\hat{M}(k_x, 0) = \begin{pmatrix} \frac{k_x}{|k_x|} & 0 \\ 0 & -\frac{|k_x|}{k_0} \end{pmatrix}. \quad (2)$$

Figure 1(a) indicates the far-field intensity $I \propto |\mathbf{E}|^2$ of a circularly polarized dipole ($\Delta\varphi = \pi/2$ and $|p_z| = |p_y|$) as a black line in the x-z plane. The emission patterns of the individual components are plotted in green (p_z) and gray (p_y). Within the chosen plane of observation, the far fields of p_z and p_y are TM (in-plane) and TE (out-of-plane) polarized. The relative phase between the dipole components is preserved, resulting in left- and right-handed circular polarization in the far field. The corresponding circularly polarized

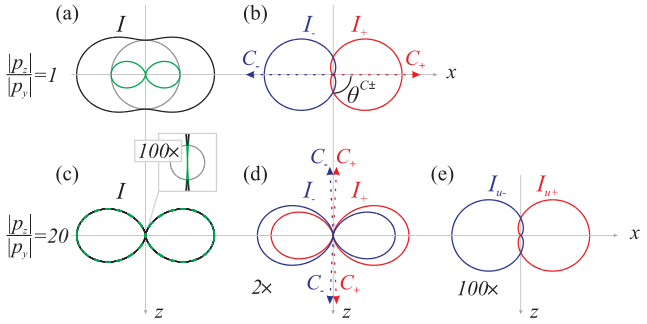

FIG. 1. Free-space far-field radiation of dipoles spinning around the x axis. The upper row corresponds to a circular polarized dipole, $|p_z|/|p_y| = 1$, with (a) showing the total far-field intensity I (black line), I_{TM} of p_z (green line), and I_{TE} of p_y (gray line). (b) Left-and right-handed circular polarization, I_- and I_+. The far-field C points ($C_\pm$) are highlighted by red and blue arrows. (c) and (d) The corresponding intensities for a strongly elliptical dipole moment, $|p_z|/|p_y| = 20$. The inset in (c) represents the central part magnified by a factor of 100, and (d) is magnified by a factor of 2. (e) Represents the far field for the postselected polarization states I_{u-} and I_{u+} magnified by 100.

intensities, $I_\pm \propto |E_{\mathrm{TE}} \pm \imath E_{\mathrm{TM}}|^2$, are plotted in red and blue in Fig. 1(b), showing strongly directional far fields with respect to the z axis. The C points are found by requiring $|E_{\mathrm{TE}}| = |E_{\mathrm{TM}}|$ [see tangent points of the green and gray curves in Fig. 1(a)]. From Eqs. (1) and (2), assuming $|p_y| \leq |p_z|$, the angles of the far-field C points can be determined by

$$k_x^{C\pm} = \pm \left| \frac{p_y}{p_z} \right| k_0. \tag{3}$$

For $|p_z| = |p_y|$, we obtain $k_x^{C\pm} = \pm k_0$, implying that the two C points of opposite helicity—C_+ and C_- highlighted by the red and blue dashed arrows in Fig. 1(b)—occur exactly on the x axis and the opening angle between the C points and the z axis is defined by $\theta^{C\pm} = |\sin^{-1}(k_x^{C\pm}/k_0)| = \pi/2$. Hence, the two C points are on opposite sides and their visibility is maximized. In contrast, when we consider an elliptically polarized dipole moment with $|p_y| < |p_z|$, we change the weightings of E_{TE} and E_{TM}. As an example, we plot the far-field intensity (solid black line), which resembles the shape of the TM-polarized component (green line), for a highly eccentric dipole—amplitude ratio $|p_z|/|p_y| = 20$—in Fig. 1(c). The magnified inset additionally shows the TE polarized component indicated in gray. Now, we find four crossing points—these are the four C points—at which the amplitudes of E_{TE} and E_{TM} match. Again, we mark $C_\pm$ as red and blue arrows in the cross sections of $I_\pm$ in Fig. 1(d). The circular polarization components exhibit a much weaker directionality in comparison to Fig. 1(b). Especially, the angle between the C points and the z axis is small, with $\theta^{C\pm} \approx 1/20$.

In the limit of $|p_y| \ll |p_z|$, the k vectors of the C points are almost aligned with the z axis, hidden in the low intensity region of the emission [see Figs. 1(c) and 1(d)]. However, it is possible to resolve the C points by using a method inspired by WM [14,16,25,29]. For that purpose, we project the far field onto a polarization state almost orthogonal to E_{TM} created by p_z, favoring E_{TE} of the weak p_y. The actual postselected polarization state $\mathbf{u}_\pm = (u_{\mathrm{TE}}, \mp u_{\mathrm{TM}})$ is optimized by choosing $u_{\mathrm{TE}} = |p_z|/|\mathbf{p}|$ and $u_{\mathrm{TM}} = \imath |p_y|/|\mathbf{p}|$, effectively compensating the amplitude difference between p_y and p_z. For the intensity pattern of the projected polarization state we obtain

$$I_{u\pm} \propto |\mathbf{E}\mathbf{u}_\pm^*|^2 = \left| \frac{k_x}{|k_x|} \pm \frac{|k_x|}{k_0} \right|^2 \frac{|p_y||p_z|}{|\mathbf{p}|^2}, \tag{4}$$

which is strongly asymmetric as shown for the example of $|p_z|/|p_y| = 20$ in Fig. 1(e). The far-field intensities $I_{u\pm}$ are identical in shape with respect to $I_\pm$ of the circular polarized dipole in Fig. 1(b), which means the visibility is maximized by the WM polarization projection, although the intensity is reduced by 2 orders of magnitude. However, the angular separation $\Delta k^{C\pm}$ and, therefore, the dipole moment ratio [see Eq. (3)] can be deduced from the directionality of the postselected polarization state.

Elliptically polarized dipoles on interface.—We consider a dipole situated in air ($z < 0$), with distance d to a glass substrate with refractive index $n = 1.5$ ($z > 0$). Because the backward emission into the air half-space is suppressed with respect to the emission into the optically denser glass [30], we concentrate on the forward direction. Considering only p_y and p_z, the far-field intensity pattern $I(k_x, k_y)$ emitted into the glass half-space is [2]

$$I(k_x, k_y) \propto \left| \begin{pmatrix} E_{\mathrm{TE}} \\ E_{\mathrm{TM}} \end{pmatrix} \right|^2 \propto |A \hat{T} \hat{M} \mathbf{p}|^2, \tag{5}$$

$$A = \sqrt{k_0^2 n^2 - k_\perp^2}/k_z e^{\imath k_z d}, \qquad \hat{T} = \begin{pmatrix} t_{\mathrm{TE}} & 0 \\ 0 & t_{\mathrm{TM}} \end{pmatrix}. \tag{6}$$

$\hat{T}(k_\perp)$ contains the Fresnel transmission coefficients t_{TE} and t_{TM}, and $A(k_\perp)$ is required for energy conservation [2]. Again, we consider the emission within the x-z plane and a spinning dipole with phase difference $\Delta\varphi = \pi/2$ between p_y and p_z. Two conditions need to be fulfilled to observe far-field C points. Firstly, $\Delta\varphi$ needs to be preserved in the far-field components E_{TE} and E_{TM}. This only holds true below the critical angle defined by $|k_x| = k_0$, since t_{TE} and t_{TM} are real for $|k_x| \leq k_0$ but complex and with different phase retardations for $|k_x| > k_0$. Secondly, the amplitudes of both field components need to be equal, $|E_{\mathrm{TE}}| = |E_{\mathrm{TM}}|$. From Eqs. (5) and (6) it follows that

$$\left| \frac{t_{\mathrm{TE}} p_y}{k_x} \right| = \left| \frac{t_{\mathrm{TM}} p_z}{k_0} \right|. \tag{7}$$

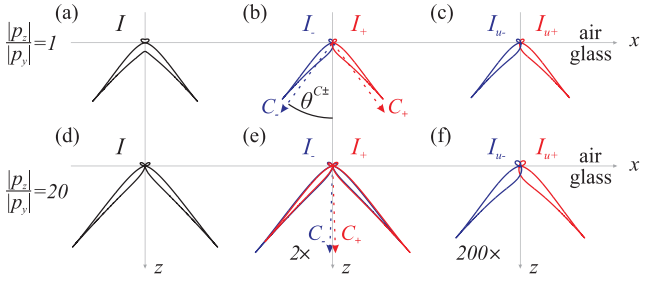

FIG. 2. Far-field radiation of dipoles spinning around the x axis above a dielectric air-glass interface. (a) and (b) Show I, I_-, and I_+ for a circular polarized dipole, with red and blue arrows highlighting $C_\pm$. (c) The corresponding postselected polarization states, I_{u-} and I_{u+}, optimized to generate perfect directionality (1:0) on the critical angle. (d)–(f) Corresponding far-field intensity patterns for a strongly elliptical dipole moment, $|p_z|/|p_y| = 20$.

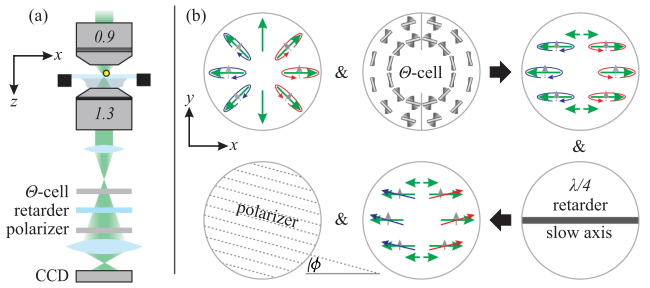

FIG. 3. Experimental setup and measurement scheme. (a) Sketch of the experimental setup. (b) Projection onto the polarization states $\mathbf{u}_\pm = [\cos(\phi), \imath \sin(\phi)]$, with $\pm$ indicating $\phi \lessgtr 0$.

By solving Eq. (7) we can calculate $k_x^{C\pm}$. For $|p_y| \ll |p_z|$, we obtain the simplified expression, $k_x^{C\pm} \approx \pm|p_y|/|p_z|k_0$, resembling Eq. (3). The angular separation is given by $\theta^{C\pm} = |\sin^{-1}(k_x^{C\pm}/nk_0)| \approx |p_y|/|p_z n|$. Besides $\theta^{C\pm}$, the intensity ratio R between the maximum intensity $I_{\max}$, which here occurs at the critical angle ($k_x = k_0$), and the intensity at the C points ($k_x = k_x^{C\pm}$) provides a practical measure of the C-point visibility:

$$R = \frac{I(k_x^{C\pm}, 0)}{I_{\max}}. \tag{8}$$

For $|p_y| \ll |p_z|$, we result in $R \approx 2|p_y|^2/(1+n)^2|p_z|^2$. Hence, only a small fraction of the light is emitted into the angular region containing the C points. The low visibility ($R \propto |p_y|^2/|p_z|^2$) combined with the small angular separation ($\theta^{C\pm} \propto |p_y|/|p_z|$) make it virtually impossible to experimentally measure the C points of highly eccentric dipoles.

We exemplarily depict the far-field intensities for a circularly polarized ($|p_z|/|p_y| = 1$) and a highly eccentric ($|p_z|/|p_y| = 20$) dipole in Figs. 2(a) and 2(d), with wavelength $\lambda = 530$ nm and distance $d = 40$ nm. The corresponding circular polarization components plotted in Figs. 2(b) and 2(e) exhibit a very strong directionality for $|p_z|/|p_y| = 1$ and a much weaker directionality for $|p_z|/|p_y| = 20$. For the circularly polarized dipole, two C points occur below but close to the critical angle at $\theta^{C\pm} \approx 0.20\pi$ with $R \approx 0.33$. In contrast, the two C points of the highly eccentric dipole appear close to the z axis. Similar to the elliptically polarized dipole in free-space [see Figs. 1(d)–1(f)], C_+ and C_- are not only barely separated in k space ($\theta^{C\pm} \approx 0.01\pi$), but also hidden in the low intensity region ($R \approx 1.5 \times 10^{-3}$). However, the visibility can be enhanced by choosing an appropriate postselected polarization state,

$$\mathbf{u}_\pm = \begin{pmatrix} u_{\mathrm{TE}} \\ \mp u_{\mathrm{TM}} \end{pmatrix} \propto \begin{pmatrix} t_{\mathrm{TM}}(k_0)|p_z| \\ \mp \imath t_{\mathrm{TE}}(k_0)|p_y| \end{pmatrix}, \tag{9}$$

which compensates the amplitude difference of E_{TE} and E_{TM} at the critical angle ($k_x = k_0$). By applying this scheme to the circular and the highly eccentric dipole moments, we obtain the far-field intensities, $I_{u\pm} \propto |\mathbf{E}\mathbf{u}_\pm^*|^2$, plotted in Figs. 2(c) and 2(f). Especially for the elliptical dipole moment, the visibility is strongly enhanced with respect to the projection onto the circular polarization basis shown in Fig. 2(e). Since the maximum of $I_{u\pm}$ is at the same angular position (critical angle) as the zero value of $I_{u\mp}$, the visibility is maximized. However, the increased visibility is reached at the cost of a reduced intensity. Nevertheless, we can use the described approach to measure hardly separated C points. Additionally, this method enables the experimental retrieval of the dipole moments themselves, which will be explained with the aid of an experimental example.

The utilized setup is sketched in Fig. 3(a). An incoming radially polarized beam ($\lambda = 530$ nm, beam width $w_0 = 1.1$ mm) focused by a microscope objective with a numerical aperture (NA) of 0.9 and focal length $f = 2.0$ mm excites a gold nanosphere with a diameter of 80 nm sitting on a glass substrate. The particle can be approximated as a dipolelike scatterer with its dipole moment being proportional to the local excitation field, $\mathbf{p} \propto \mathbf{E}$ [31]. When the particle is in the center of the focal spot, we induce a p_z dipole moment [9]. However, a subwavelength shift of the particle along the y direction induces an additional weak p_y dipole component [9]. The relative phase between p_z and p_y is close to $\pm\pi/2$, because of the transverse spin arising in tightly focused radially polarized beams [9,32]. The ratio of the dipole amplitudes is controlled by the distance between the particle and the center of the focal spot [9]. The light scattered into the glass substrate is collected by an immersion-type objective (NA = 1.3) in confocal configuration. Behind the objective, we project the polarization of the scattered light onto $\mathbf{u}_\pm$. For that, we image the back focal plane of the lower

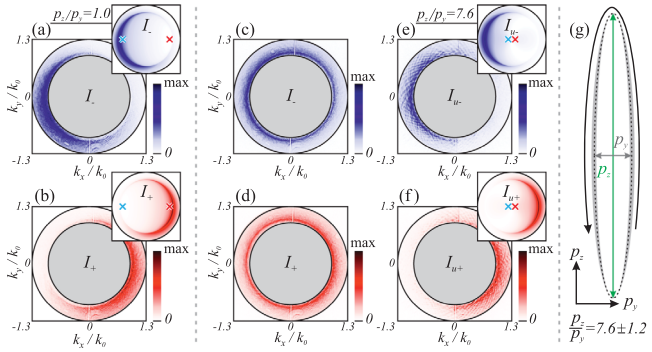

FIG. 4. Polarization-resolved back focal plane (BFP) images. (a) and (b) I_- and I_+ distributions (normalized to their common maximum, depicted angular range defined by $0.95 \leq k_\perp/k_0 \leq 1.3$) for a particle position of $x \approx 0$ and $y \approx 200$ nm, where $|p_z|/|p_y| \approx 1$. Theoretical distributions are shown as insets (red and blue crosses indicate the C points). (c) and (d) I_- and I_+ for $x \approx 0$ and $y \approx 30$ nm. (e) and (f) BFP images for the same position as (c) and (d), but for a postselected polarization state of $\mathbf{u}_\pm = [\cos(\phi), \imath \sin(\phi)]$ with $\phi = \mp 5°$. Theoretical distributions including the reconstructed C points are shown as insets. (g) The dashed black line indicates the reconstructed polarization ellipse, with error margins, spin, and dipole moments indicated as gray background, black vector, and green (p_z) and gray (p_y) vectors, respectively.

objective onto a Θ cell containing liquid crystals, which locally rotate the incoming polarization state [33]. This converts E_{TE} and E_{TM} to E_y and E_x. Additionally, the Θ cell introduces a small phase shift between E_{TE} and E_{TM}, which can be neglected in this proof-of-principle experiment. For illustration, the effect of the Θ cell is sketched in Fig. 3(b). In front of the Θ cell, the light is mainly TM polarized (green arrows) with only a weak $\pm\pi/2$ phase-shifted TE component (gray arrows). The TM component is symmetric with respect to the optical axis (z axis) and the TE component is antisymmetric with respect to the y axis. This exemplary polarization state is chosen for this discussion, since it is similar to the expected left- and right-handed elliptically polarized far fields (see red and blue arrows) of a spinning dipole [11]. The local polarization rotation of the Θ cell is sketched in gray. The polarization distribution behind the Θ cell is sketched on the right, with E_{TM} and E_{TE} being converted into E_x and E_y. A $\lambda/4$ retarder transforms the locally elliptical polarization distribution into purely linear polarization with varying orientation of the polarization axis. Utilizing a linear polarizer set to an angle ϕ with respect to the x axis, we realize the projection onto the polarization state $\mathbf{u}_\pm = [\cos(\phi), \imath \sin(\phi)]$, where the index $\pm$ indicates $\phi \lessgtr 0$.

Finally, we experimentally investigate the emission patterns for two different particle positions. In Figs. 4(a) and 4(b), we depict the circularly polarized far fields I_- and I_+ for a particle position of $x \approx 0$ and $y \approx 200$ nm, where we expect the induced dipole moment to be nearly circular [9]. We measure the scattered light only within the angular range defined by $0.95 \leq k_\perp/k_0 \leq 1.3$ (see black circles), since the immersion-type objective has an NA of 1.3 and below $k_\perp/k_0 = 0.9$ the scattered light interferes with the much stronger excitation beam (the angular region below $k_\perp/k_0 = 0.95$ is indicated as gray area). For comparison, we depict the theoretical distributions as insets, calculated for $\Delta\varphi = \pi/2$ and $|p_y| = |p_z|$. As mentioned above, the C points occur slightly below the critical angle (see red and blue crosses). Experiment and theory are in very good agreement, indicating that the experimentally excited dipole closely resembles the theoretically assumed dipole moment.

Now, we position the particle at $x \approx 0$ and $y \approx 30$ nm, obtaining I_- and I_+ as they are depicted in Figs. 4(c) and 4(d). Here, p_z dominates p_y [5], and in comparison to Figs. 4(a) and 4(b), the spin splitting is much weaker and the C points would be barely separated and hard to observe. Actually, within our experimental geometry, the C points cannot be measured at all, since they are in the angular region far below NA = 0.9 (see gray area), where the scattered light is interfering with the transmitted excitation beam. However, it is possible to determine the position of these C points of the scattered light by adjusting the angle of the polarizer to reach maximum visibility at the critical angle. Here, we obtain the strongly directional far fields in Figs. 4(e) and 4(f) for a polarizer angle of $\phi \approx 5°$. The reduced intensity of the scattered light is compensated by a longer exposure time of the camera [fluctuations in Figs. 4(e) and 4(f) are caused by imperfections of the polarization projection]. By comparing the experimental post-selected polarization state $\mathbf{u}_\pm = [\cos(5°), \mp \imath \sin(5°)]$ with Eq. (9) we can determine the positions of the C points, the dipole moment amplitude ratio $|p_z|/|p_y| \approx 7.6 \pm 1.2$, and the sign of the spin, here pointing in positive x direction [32]. The result is illustrated as a polarization ellipse (dashed black line) in Fig. 4(g), where the margin of error is indicated as the gray area, the long and short axis of the dipole are shown as green and gray vectors, and the spinning direction is sketched as a black vector. The good overlap between experiment and theory (insets) in Figs. 4(e) and 4(f)—calculated for $|p_z|/|p_y| = 7.6$, with C points marked for the sake of completeness—indirectly validates the experimental postselection technique [25].

Conclusion.—We established a link between the elliptical polarization of a dipole emitter and its far-field C points. Furthermore, we theoretically and experimentally demonstrated that projecting the far field onto a spatially varying postselected polarization state reveals the angular separation and the helicities of C points even for highly eccentric dipole moments, enabling the experimental retrieval of their complex dipole moments.

In principle, the technique can be adapted to measure the orientation of linear dipoles [25], an important task in nanophotonics and microscopy [34–38], where the

orientation of transition dipole moments of quantum emitters in anisotropic environments influences the lifetime of their excited states [39,40]. Moreover, the robustness of our technique to noise [25] may allow for localizing of nanoparticles with subwavelength precision [5] and for distinguishing adjacent quantum emitters with slightly different dipole moments.

To compare our results with a BFP fitting technique that measures the orientation of molecules exhibiting linear dipole moments [35], we express our accuracy in degree using the reconstructed dipole moment including the error margins: $\Delta = \pm[\tan^{-1}(8.8) - \tan^{-1}(6.4)]/2 \approx \pm 1.2°$, which is comparable to the accuracy of 1°–2° reported in Ref. [35]. Even higher accuracies can be achieved using scanning methods [36,41], which could be combined with the presented polarization projection technique.

An advantage of the WM scheme is that only a small portion of the light is used to detect the orientation of the dipole. While in our proof-of-principle experiment the remaining light is dumped by the polarization filter, it could be used, for instance, to gain spectral information on the dipole emitter.

The authors gratefully acknowledge fruitful discussions with Yuri Gorodetski. M. N. acknowledges financial support from the European Union's Horizon 2020 Research and Innovation Program (Q-SORT), Grant No. 766970.

*S. N. and M. N. authors contributed equally
†peter.banzer@mpl.mpg.de
http://www.mpl.mpg.de/

[1] P. Michler, A. Kiraz, C. Becher, W. V. Schoenfeld, P. M. Petroff, L. Zhang, E. Hu, and A. Imamoglu, Science **290**, 2282 (2000).
[2] L. Novotny and B. Hecht, *Principles of Nano-Optics*, 2nd ed. (Cambridge University Press, Cambridge, England, 2006), DOI: 10.1017/CBO9780511794193.
[3] S. Weisenburger, B. Jing, D. Hänni, L. Reymond, B. Schuler, A. Renn, and V. Sandoghdar, ChemPhysChem **15**, 763 (2014).
[4] N. Rotenberg and L. Kuipers, Nat. Photonics **8**, 919 (2014).
[5] M. Neugebauer, P. Woźniak, A. Bag, G. Leuchs, and P. Banzer, Nat. Commun. **7**, 11286 (2016).
[6] M. Decker, I. Staude, M. Falkner, J. Dominguez, D. N. Neshev, I. Brener, T. Pertsch, and Y. S. Kivshar, Adv. Opt. Mater. **3**, 813 (2015).
[7] A. Aiello, P. Banzer, M. Neugebauer, and G. Leuchs, Nat. Photonics **9**, 789 (2015).
[8] K. Y. Bliokh, F. J. Rodríguez-Fortuño, F. Nori, and A. V. Zayats, Nat. Photonics **9**, 796 (2015).
[9] M. Neugebauer, T. Bauer, P. Banzer, and G. Leuchs, Nano Lett. **14**, 2546 (2014).
[10] J. Petersen, J. Volz, and A. Rauschenbeutel, Science **346**, 67 (2014).
[11] O. G. Rodríguez-Herrera, D. Lara, K. Y. Bliokh, E. A. Ostrovskaya, and C. Dainty, Phys. Rev. Lett. **104**, 253601 (2010).
[12] D. O'Connor, P. Ginzburg, F. J. Rodríguez-Fortuño, G. A. Wurtz, and A. V. Zayats, Nat. Commun. **5**, 5327 (2014).
[13] J. F. Nye, Proc. R. Soc. A **389**, 279 (1983).
[14] Y. Aharonov, D. Z. Albert, and L. Vaidman, Phys. Rev. Lett. **60**, 1351 (1988).
[15] I. M. Duck, P. M. Stevenson, and E. C. G. Sudarshan, Phys. Rev. D **40**, 2112 (1989).
[16] O. Hosten and P. Kwiat, Science **319**, 787 (2008).
[17] M. R. Dennis and J. B. Götte, New J. Phys. **14**, 073013 (2012).
[18] Y. Gorodetski, K. Y. Bliokh, B. Stein, C. Genet, N. Shitrit, V. Kleiner, E. Hasman, and T. W. Ebbesen, Phys. Rev. Lett. **109**, 013901 (2012).
[19] O. S. Magaña-Loaiza, M. Mirhosseini, B. Rodenburg, and R. W. Boyd, Phys. Rev. Lett. **112**, 200401 (2014).
[20] M. Mirhosseini, O. S. Magaña-Loaiza, C. Chen, S. M. Hashemi Rafsanjani, and R. W. Boyd, Phys. Rev. Lett. **116**, 130402 (2016).
[21] Postselection in optics is used in different contexts: It relates to correlated modes and conditioning (e.g., heralded single photon sources [22]), and to correlated properties in one mode (e.g., strong interference of orthogonally polarized fields by polarization projection [16–18]). The usage here refers to the latter.
[22] P. Kok, W. J. Munro, K. Nemoto, T. C. Ralph, J. P. Dowling, and G. J. Milburn, Rev. Mod. Phys. **79**, 135 (2007).
[23] J. D. Jackson, *Classical Electrodynamics*, 3rd ed. (Wiley, New York, 1999).
[24] M. Neugebauer, J. S. Eismann, T. Bauer, and P. Banzer, Phys. Rev. X **8**, 021042 (2018).
[25] See Supplemental Material at http://link.aps.org/supplemental/10.1103/PhysRevLett.121.243903 for the derivation of Eq. (1), which includes Ref. [26], for a formal description of the optical weak measurement scheme, which includes Refs. [27,28], for measuring the orientation of linearly polarized dipoles, and for a theoretical estimation of the excited dipole moment.
[26] J. Y. Courtois, J. M. Courty, and J. C. Mertz, Phys. Rev. A **53**, 1862 (1996).
[27] G. Puentes, N. Hermosa, and J. P. Torres, Phys. Rev. Lett. **109**, 040401 (2012).
[28] I. Fernandez-Corbaton, X. Zambrana-Puyalto, and G. Molina-Terriza, Phys. Rev. A **86**, 042103 (2012).
[29] J. Dressel, Phys. Rev. A **91**, 032116 (2015).
[30] W. Lukosz and R. E. Kunz, J. Opt. Soc. Am. **67**, 1615 (1977).
[31] K. G. Lee, H. W. Kihm, J. E. Kihm, W. J. Choi, H. Kim, C. Ropers, D. J. Park, Y. C. Yoon, S. B. Choi, D. H. Woo, J. Kim, B. Lee, Q. H. Park, C. Lienau, and D. S. Kim, Nat. Photonics **1**, 53 (2007).
[32] M. Neugebauer, T. Bauer, A. Aiello, and P. Banzer, Phys. Rev. Lett. **114**, 063901 (2015).
[33] M. Stalder and M. Schadt, Opt. Lett. **21**, 1948 (1996).
[34] M. Böhmer and J. Enderlein, J. Opt. Soc. Am. B **20**, 554 (2003).
[35] M. A. Lieb, J. M. Zavislan, and L. Novotny, J. Opt. Soc. Am. B **21**, 1210 (2004).
[36] N. Karedla, S. C. Stein, D. Hähnel, I. Gregor, A. Chizhik, and J. Enderlein, Phys. Rev. Lett. **115**, 173002 (2015).

[37] D. Patra, I. Gregor, and J. Enderlein, J. Phys. Chem. A **108**, 6836 (2004).
[38] M. R. Foreman, C. M. Romero, and P. Török, Opt. Lett. **33**, 1020 (2008).
[39] R. E. Kunz and W. Lukosz, Phys. Rev. B **21**, 4814 (1980).
[40] P. Lodahl, S. Mahmoodian, and S. Stobbe, Rev. Mod. Phys. **87**, 347 (2015).
[41] N. Karedla, Single-molecule transition dipole imaging, in *Single-Molecule Metal-Induced Energy Transfer: From Basics to Applications* (Springer International Publishing, Cham, 2017), pp. 87–143, DOI: 10.1007/978-3-319-60537-1_4.